Remote Sensing of Environment 256 (2021) 112341

Contents lists available at ScienceDirect

Remote Sensing of Environment

journal homepage: www.elsevier.com/locate/rse

# Quantifying Surface Melt and Liquid Water on the Greenland Ice Sheet using L-band Radiometry

Derek Houtz [a,*], Christian Mätzler [b], Reza Naderpour [a], Mike Schwank [a,b], Konrad Steffen [a]

[a] Swiss Federal Institute for Forest, Snow and Landscape Research, Zürcherstrasse 111, 8903 Birmensdorf, CH, Switzerland
[b] Gamma Remote Sensing AG, Worbstrasse 225, 3073, Muri, bei Bern, CH, Switzerland

ABSTRACT:

Understanding surface melt over the Greenland Ice Sheet (GrIS) is important for evaluating the effect of the changing global climate on humanity, and for forecasting sea level rise. We demonstrate a recently developed L-band passive microwave algorithm for the retrieval of snow liquid water and snow and firn density over the GrIS. The retrievals are performed using brightness temperatures from the ESA SMOS satellite. The density retrievals show potential for mapping the equilibrium line altitude of the ice sheet by determining where retrieved densities exceed typical seasonal snowpack density, thus indicating the presence of firn. We integrate snow liquid water retrievals over area and time to obtain water column maps and daily estimates of the surface liquid water present over Greenland. The integrated annual surface liquid water retrieved over the entire ice sheet compares on the same order as modeled estimates of total meltwater available in current literature.

## 1. Introduction

Global sea levels are rising, and current predictions suggest that the rate of sea level rise will continue to accelerate (Kopp et al. 2016; Nerem et al. 2018). Mass loss of the Greenland Ice Sheet (GrIS) currently contributes about 0.72 mm/yr to global sea level rise (Forsberg et al. 2017), and along with Antarctica, is predicted to become the dominant contributor to global sea level rise within the century (Golledge et al. 2019). The mass balance quantifies the total mass change of the GrIS and is directly proportional to mean global sea level. It has been shown that the rate of GrIS mass loss is increasing and could contribute to 7-21 cm increase in Global Mean Sea Level (GMSL) by the end of the century (Oppenheimer et al. 2019).

Both the Surface Mass Balance (SMB) and glacier discharge (ice deposited from outlet glaciers directly into the ocean) contribute significantly to the mass balance of the GrIS, and the two are correlated (Rignot et al. 2008). The SMB includes positive mass contributions from precipitation as well as loss due to evaporation and sublimation in addition to the dominant meltwater runoff loss (van den Broeke et al. 2017). The mass balance can be summarized by,

$$\begin{aligned} Mass\,Balance &= SMB - Discharge \text{ and } SMB \\ &= Precipiation - Meltwater\,Runoff - Sublimation - Evaporation. \end{aligned} \tag{1}$$

Current forecasts, which include uncertainties in basal friction, the lubrication of discharging ice, suggest large uncertainty in the future Greenland mass balance (Gillet-Chaulet et al. 2012). Accurate knowledge of the current state of the GrIS SMB is thus imperative to predict the possible rate of future global sea level rise. Surface mass loss is expected to increase significantly in the 21st century, compared to discharge, and the SMB is the dominant contributor to uncertainty in GMSL predictions (Oppenheimer et al. 2019).

One of the most direct methods of measuring mass change is by gravimetry from the Gravity Recovery and Climate Experiment (GRACE) satellite (Velicogna and Wahr 2005). GRACE-derived estimates have their own sources of uncertainty, particularly glacier isostatic adjustment or postglacial rebound (Barletta et al. 2008; van der Wal et al. 2015) and tidal aliasing (Moore and King 2008). Also GRACE measurements typically need more than 5 years of integration to achieve sufficiently accurate estimates of GrIS mass-change (Luo et al. 2012). Mass balance can also be studied from laser or radar altimetry but these techniques also have uncertainties introduced by the required knowledge on density distribution over the GrIS (Hurkmans et al. 2014).

Satellite data have been used to map surface melt on the GrIS, particularly passive microwave (Abdalati and Steffen 1995; Abdalati and Steffen 1997), radar backscatter (Nghiem et al. 2001), and visible imagery (Hall et al. 2013). However, these methods only provide maps of binary information on melt versus non-melt, and are unable to provide quantitative information about volumetric liquid water. In Houtz

* Corresponding author.
E-mail addresses: Derek.Houtz@WSL.ch (D. Houtz), Matzler@gamma-rs.ch (C. Mätzler), Reza.Naderpour@WSL.ch (R. Naderpour), Mike.Schwank@WSL.ch (M. Schwank), Konrad.Steffen@WSL.ch (K. Steffen).

https://doi.org/10.1016/j.rse.2021.112341
Received 8 June 2020; Received in revised form 10 December 2020; Accepted 2 February 2021
Available online 12 February 2021
0034-4257/© 2021 The Author(s). Published by Elsevier Inc. This is an open access article under the CC BY license (http://creativecommons.org/licenses/by/4.0/).

et al. (2019) a new method was introduced for the simultaneous retrieval of snow/firn mass-density and snow liquid water content from passive L-band radiometry. Its suitability was demonstrated for the period 2011 – 2018 at the "Swiss Camp" (Steffen 1995) research site in the ablation zone, near the Equilibrium Line Altitude (ELA), in Western Greenland northeast of the Jacobshavn Isbrae. In this study, we expand corresponding retrievals to the entire GrIS, and show: density, liquid water column, and integrated surface liquid water estimates.

Microwave brightness temperatures measured at 1.4 GHz by the European Space Agency (ESA) Soil Moisture and Ocean Salinity (SMOS) satellite (Kerr et al. 2001) (level 3 gridded (Al Bitar et al. 2017)) are the sole input to our retrieval algorithm. We show that liquid water column, down to the penetration depth of L-band microwaves, can be calculated from SMOS-based retrievals using a physically deterministic Emission Model (EM). By integrating retrieved liquid water over time and area we estimate the volume of melt water on the GrIS as a function of time and as an annual total. We discuss how this quantified total melt water relates to the GrIS surface mass loss and thus to the SMB, and we also discuss the limitations of the algorithm and uncertainty contributions.

We first introduce the details of the retrieval approach specific to this study, and the satellite datasets used for comparison. Second, we present and discuss results of the density retrieval, liquid water column and integrated liquid water. Finally, we highlight important conclusions, and motivate future research.

## 2. Approaches and Datasets

### 2.1. Snow liquid water content and density retrieval

The approach used in this study to retrieve volumetric liquid water-content and firn/snow mass-density, $W_S$, $\rho_S$ respectively, involves the two-layer configuration of the L-band Specific Microwave Emission Model of Layered Snowpacks (LS-MEMLS) (Schwank et al. 2014). LS-MEMLS is used to simulate (sim) brightness temperatures $T_{B,\,\mathrm{sim}}^{p,\theta_j}$ of the firn/snow atop the substrate (represented by an infinite half-space of glacial ice) at horizontal and vertical polarization $p = \{H, V\}$ at nadir observation angles $\theta_j$. The same Emission Model (EM) was used in Houtz et al. 2019. Therefore, a detailed outline of the EM is omitted and the reader is referred to Houtz et al. 2019 for detailed information on the EM. Nevertheless, Fig. 1 sketches the considered configuration of LS-MEMLS, and Table 1 recaps the most relevant EM parameters including their symbols, units, and values or equation numbers used in Houtz et al. 2019. We still assume specular reflections on all interfaces, and the dry snow is considered lossless. The EM is incoherent (coherent effects are assumed to be averaged out over 25 km pixels (Schwank et al. 2014)), such that the dry snow thickness has no impact on the simulated brightness temperatures.

Retrievals $(W_S, \rho_S)$ are derived by optimally matching simulated $T_{B,\,\mathrm{sim}}^{p,\theta_j}(W_S, \rho_S)$ to SMOS Level-3 (L3) Bottom-of-Atmosphere (BA) brightness temperatures $T_{B,\,\mathrm{BA}}^{p,\theta_j}$ by minimizing the Cost Function (*CF*):

$$CF(W_S, \rho_S) = \sum_{\substack{j=1 \\ p=\{H,V\}}}^{n} \frac{\left(T_{B,BA}^{p,\theta_j} - T_{B,sim}^{p,\theta_j}(W_S, \rho_S)\right)^2}{\left[\triangle T_B^{p,\theta_j}\right]^2} \tag{2}$$

$\triangle T_{B,\,\mathrm{BA}}^{p,\,\theta_j}$ is a weighting term, equal to the total uncertainty of each SMOS $T_{B,\,\mathrm{BA}}^{p,\,\theta_j}$. $\triangle T_B^{p,\,\theta_j}$ is the root sum square of instrumental radiometric uncertainty (~3 K) and incidence angle dependent standard deviations resulting from the angle binning process described in (Al Bitar et al. 2017), and has values ranging between about 4 K and 10 K depending on incidence angle and polarization. This weighting formulation assumes that the model uncertainties are negligible compared to the measurement uncertainty. Minimization of the *CF* is achieved using a two-dimensional numerical minimization routine. The values of $(W_S, \rho_S)$ for which *CF* reaches its global minimum are considered as the retrievals. A detailed investigation of various measurements and resulting retrievals showed that the $(W_S, \rho_S)$ pair that minimizes *CF* are a unique solution pair and there is only one global minimum.

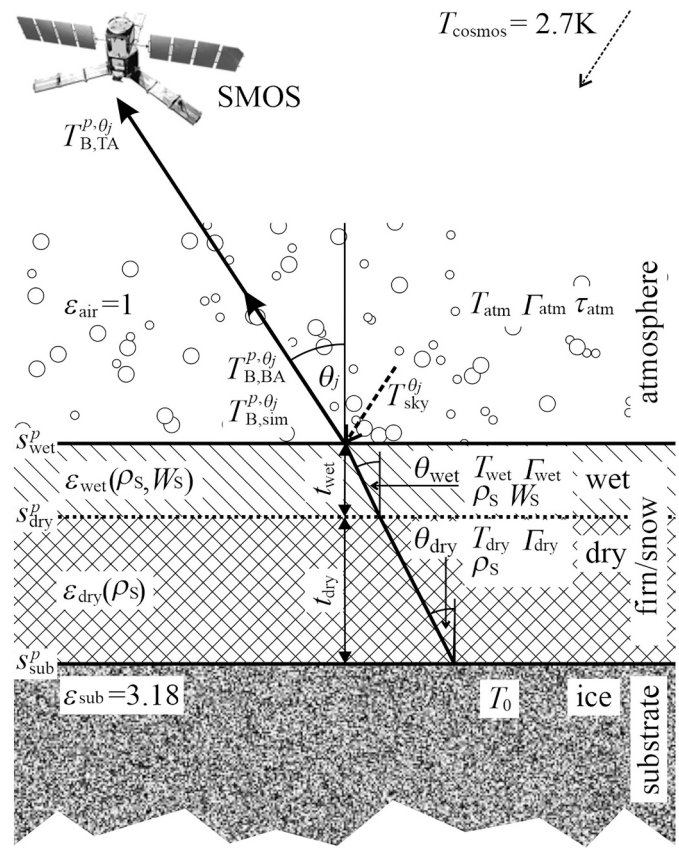


**Fig. 1.** Configuration of the L-band Specific microwave Emission Model (LS-MEMLS) used in the retrieval of $(W_S, \rho_S)$ over the Greenland Ice Sheet (GrIS). Symbols are explained in Table 1.

An investigation was also performed, similar to that of Naderpour et al., 2017, to determine whether the use of both polarizations $p = \{H, V\}$ is required, or whether a single polarization mode can provide valid retrievals. The algorithm was run with $p = H$ and $p = V$ only. It was found that use of a single polarization greatly increases the overall noise and number of false positive $W_S$ retrievals and thus the combined $p = \{H, V\}$ is used in the *CF* calculation.

This $(W_S, \rho_S)$ retrieval approach was first introduced in Houtz et al. 2019 and validated over the "Swiss Camp" research site in the western Greenland ablation zone including comparisons to in-situ data and the cross-polarized gradient ratio (XPGR) method (Abdalati and Steffen 1995). The approach was further validated using ground-based radiometry in Naderpour et al. 2020. We apply the identical retrieval approach in this study over the entire GrIS. The resulting SMOS-based $W_S$ retrievals are used to quantify liquid water over the GrIS resulting from surface melt of the uppermost firn/snow layer. The employed approach is outlined in the subsequent Section 2. 2. Furthermore, we investigate sensitivities of the GrIS melt-water derived from $W_S$ retrievals with respect to $t_{\mathrm{wet}}$, the sole non-deterministic parameter. In Houtz et al. 2019 only $t_{\mathrm{wet}} = 0.1$ m was considered, whereas here we investigate $t_{\mathrm{wet}} = \{0.1, 0.3, 0.6, 1.0\}$ m. A further difference compared to Houtz et al. 2019 is the way in which the upwelling substrate brightness temperature $T_0$ is estimated ($T_{\mathrm{sub}}$ in Houtz et al. 2019). Here, $T_0$ is computed for each year individually, as opposed to the multi-year mean used in Houtz et al. 2019, to demonstrate a more operationally-ready algorithm. Single-year averages of near-Brewster angle vertical polarization brightness temperatures are used to assess $T_0$, as opposed to the 8

**Table 1**
LS-MEMLS symbols used in Fig. 1, including their units, meaning, and values or equation numbers used in Houtz et al. 2019.

| symbol | unit | description | value/equation |
|---|---|---|---|
| $W_S$ | $m^3m^{-3}$ | snow volumetric liquid water-content | retrieval parameter |
| $\rho_S$ | kg $m^{-3}$ | mass-density of dry firn/snow layers | retrieval parameter |
| $p$ | - | horizontal and vertical polarization | {H, V} |
| $\theta_j$ | degrees | observation angle relative to nadir | SMOS level-3 |
| $T^{p,\theta_j}_{B,BA}$ | K | Bottom-of-Atmosphere (BA) brightness temperature | (Houtz et al. 2019) Eq. (14) |
| $T^{p,\theta_j}_{B,TA}$ | K | Top-of-Atmosphere (TA) brightness temperature | (Houtz et al. 2019) Eq. (14) |
| $T^{p,\theta_j}_{B,sim}$ | K | simulated BA brightness temperature | (Houtz et al. 2019) Eq. (3) |
| $\varepsilon_{sub}$ | - | permittivity of substrate (real) | 3.18 |
| $\varepsilon_{dry}$ | - | permittivity of dry firn/snow (real) | (Houtz et al. 2019) Eq. (9) |
| $\varepsilon_{wet}$ | - | permittivity of wet snow (complex) | (Houtz et al. 2019) Eq. (8) |
| $\varepsilon_{air}$ | - | permittivity of air/vacuum | 1 |
| $s^p_{sub}$ | | reflectivity of upper interface of substrate | (Houtz et al. 2019) Eq. (5) |
| $s^p_{wet}$ | - | reflectivity of upper interface of wet snow-layer | (Houtz et al. 2019) Eq. (5) |
| $s^p_{dry}$ | - | reflectivity of upper interface of dry snow-layer | (Houtz et al. 2019) Eq. (5) |
| $\Gamma_{wet}$ | - | transmissivity of wet snow-layer | (Houtz et al. 2019) Eq. (7) |
| $\Gamma_{dry}$ | - | transmissivity of dry firn/snow-layer | 1 |
| $\Gamma_{atm}$ | - | atmospheric transmissivity | (Houtz et al. 2019) Eq. (11) |
| $t_{wet}$ | m | thickness of wet snow-layer | {0.1, 0.3, 0.6, 1.0} |
| $t_{dry}$ | m | thickness of dry snow-layer | irrelevant, $\Gamma_{dry} = 1$ |
| $T_0$ | K | upwelling brightness temperature of substrate | Eq. (3) |
| $T_{dry}$ | K | temperature of dry firn/snow-layer | irrelevant |
| $T_{wet}$ | K | temperature of wet snow-layer | 273.15 |
| $\theta_{wet}$ | degrees | propagation angle in wet snow-layer | (Houtz et al. 2019) Eq. (6) |
| $\theta_{dry}$ | degrees | propagation angle in dry firn/snow-layer | (Houtz et al. 2019) Eq. (6) |
| $T^{\theta_j}_{sky}$ | K | brightness temperature of sky below atmosphere | (Houtz et al. 2019) Eq. (10) |
| $T_{cosmos}$ | K | cosmic microwave background radiation | 2.7 |
| $T_{atm}$ | K | effective temperature of the atmosphere | (Houtz et al. 2019) Eq. (11) |
| $\tau_{atm}$ | - | optical depth of atmosphere | (Houtz et al. 2019) Eq. (11) |

year average that was used in Houtz et al. 2019. The Brewster angle between dry snow and ice represents the angle of maximum emissivity of the ice. At vertical polarization, and during dry snow periods, the impact of the snow is also minimized, as justified in Houtz et al. 2019, and discussed in Mätzler 2001. We also only consider a period in the assumed dry snow period (the first 90 Days of the Year (DoY)) in which we assume the firn/snow to be dry, as surface wetness can significantly increase the firn/snow permittivity and therefore change the Brewster angle. $T_0$ is given as,

$$T_0 \approx \left\langle T^{V,\theta_j=\{52.5^\circ,57.5^\circ\}}_{B,BA} \right\rangle_{DoY=\{1-90\}}. \tag{3}$$

where $T^{V,\theta_j}_{B,BA}$ are the SMOS Bottom-of-Atmosphere (BA) vertical polarization ($p$ = V) brightness temperatures near the Brewster angle, $\theta_{Brewster} = tan^{-1}\left(\sqrt{\varepsilon_{sub}}/\sqrt{\varepsilon_{dry}}\right) \approx \theta_j = \{52.5^\circ, 57.5^\circ\}$ estimated for $\varepsilon_{dry} = 1.5$ and $\varepsilon_{sub} = 3.18$ (Fig. 1). DoY = {1 − 90} indicates the annual time-period for which the snow/firn is considered to be dry.

### 2.2. Water column and integrated liquid water calculations

The penetration depth of L-band microwaves is highly sensitive to liquid water but is on the order of decimeters for moist snow with ~5% snow liquid water content (Mätzler et al. 1984) and this depth increases with decreasing water content and vice versa. L-band penetration depth into the snow/ice of the GrIS also varies significantly depending on the regions. Ranging from a few to tens of meters in regions experiencing melt, due to increased reflectivity of melt facies and density variations (Macelloni et al., 2016), up to 60-120 m in the cold and dry Northeast regions of the ice sheet (Rignot et al. 2001). The liquid water column down to the penetration depth of L-band can be calculated from the volumetric snow liquid water content $W_S$ (units of $m^3m^{-3}$) and the wet layer thickness $t_{wet}$ (units of m). For a SMOS orbit $i$ the instantaneous water column at a single pixel $W_{c,\ i}$ can be calculated as:

$$W_{c,i} = W_S \cdot t_{wet}. \tag{4}$$

We then make some simplifying assumptions to proceed with the spatial and temporal analyses. We assume, i) that the liquid water detected in a single orbit percolates down below the penetration depth of L-band, or refreezes, in one day, ii) that all liquid water newly formed between two overpasses is detected on the latter satellite overpass. The instantaneous water column $W_{c,\ i}$ can now be summed over all observations, and normalized by the number of observations, to obtain annual (yr) liquid water column $W_{c,\ yr}$,

$$W_{c,yr} = \frac{n_{days}}{n^{yr}_{obs}} \sum_{i=1}^{n^{yr}_{obs}} W_{c,i} \tag{5}$$

where $n^{yr}_{obs}$ is the total number of ascending and descending SMOS observations over a given pixel in a year (yr), and $n_{days}$ is the number of days in a year (365 or 366 for leap years). $n^{yr}_{obs}$ can vary from pixel to pixel and from year to year depending on SMOS level 3 data processing, filtering and gridding. Note that error in above assumption (i) will cause multiple detections of the same liquid water volume and thus an overestimation of $W_{c,\ yr}$, whereas error in above assumption (ii) will miss detection of liquid water, and thus cause an underestimation of $W_{c,yr}$. Assumption (i) is partially justified by Samimi and Marshall 2017 where a vertical drainage rate of greater than 20 cm per hour was observed, and it is shown that over a 24-hour timescale, all meltwater drains below the ~40 cm sensing depth at L-band, even in the early melt season. These opposing error effects are discussed in further detail in Section 3. The value of $W_{c,\ yr}$ is computed for each GrIS pixel on the SMOS Equal-Area Scalable Earth version 2.0 grid (EASE-grid 2.0) (Brodzik et al. 2012).

We can conveniently use the EASE-grid 2.0 projection to compute the total volume (or mass) of liquid water present on the ice sheet, and within the L-band penetration depth, on any day or averaged over a year. The daily integrated liquid water over the entire ice sheet is given as,

$$W_{day} = \frac{A_{pixel} \cdot n_{pixels}}{n^{day}_{obs}} \sum_{i=1}^{n^{day}_{obs}} W_{c,i} \tag{6}$$

where $A_{pixel}$ is the area of one pixel, or $A_{pixel} \simeq 25.025$ km × 25.025 km $\simeq 626.250625 \cdot 10^6$ $m^2$ for the SMOS EASE-grid 2.0, $n^{day}_{obs}$ is the total number of ascending and descending observations over all pixels within

the ice sheet mask observed on a single day, and $n_{\text{pixels}}$ is the total number of SMOS pixels lying fully within the ice sheet mask. Accordingly, these daily total liquid water estimates can be summed to calculate the annual liquid water detected on the GrIS,

$$W_{\text{yr}} = \sum^{W_{\text{day}} > \sigma} W_{\text{day}}. \tag{7}$$

Note that there is no normalization or $n_{\text{obs}}^{\text{yr}}$ required here because there are observations of $W_{\text{day}}$ for at least a fraction of the ice sheet on every day of the year, and normalization by $n_{\text{obs}}^{\text{day}}$ has already corrected for this fraction. The factor $\sigma$ is the mean noise level of $W_{\text{day}}$ for each year calculated assuming dry snow during the first 90 Days of the Year (DoY) similarly to *T*0,

$$\sigma = \langle W_{\text{day}} \rangle_{\text{DoY}=\{1-90\}}. \tag{8}$$

The value $\sigma$ accounts for perennial liquid water detected by SMOS during the dry snow period, which could include subsurface firn aquifers (Brangers et al. 2020; Miège et al. 2016) or firn-suspended liquid water down to the penetration depth of L-band in the GrIS. The spatial variations of $\sigma$ can also be examined by calculating the dry snow period liquid water column $W_{\text{c, DoY}=\{1-90\}}$ by performing the sum of Eq. (5) with $n_{\text{obs}}^{\text{yr}}$ replaced with $n_{\text{obs}}^{\text{DoY}=\{1-90\}}$, total number of ascending and descending SMOS observations over a given pixel in the first 90 days of the year, and $n_{\text{days}}$ in this case is 90.

This $\sigma$ term also aims to remove false positive liquid water retrievals from the annual sums. False positives can result from highly reflective layered melt facies in the percolation and melt zones. A recent investigation has demonstrated the ability of using NASA Soil Moisture Active Passive (SMAP) (Entekhabi et al. 2010) L-band radiometer data to identify sub-surface perennial firn aquifers (Miller et al. 2020). Initial investigations show some potential for our SMOS-based algorithm to also detect perennial firn aquifers, but there are some suspected false positive liquid water retrievals particularly around the Jacobshavn outlet glacier.

$W_s$ as volume fraction of liquid water is intrinsically unitless, or with units of $m^3m^{-3}$. When multiplied by $t_{\text{wet}}$, in units of m. we obtain $W_{\text{c, }i}$, also in m. Multiplying the water column in units of m by the total area observed in $m^2$ yields liquid water volume in units of $m^3$. We can convert liquid water in $m^3$ to mass by multiplying by the density of water, 1000 kg $m^{-3}$. Following the convention frequently used in surface-mass-balance studies, we present pan ice-sheet liquid water mass in units of Gt.

### 2.3. SMOS data

Retrievals ($W_S, \rho_S$) of snow liquid water-content and snow density are derived from multi-angle dual-polarization Level-3 (L3) gridded brightness temperatures $T_{\text{B, TA}}^{p,\,\theta_j}$ measured at the Top-of-Atmosphere (TA) by SMOS (Al Bitar et al. 2017). The data used spans the period between 1 January 2011 and 31 December 2018. These data are provided in separate ascending and descending pass NetCDF files and are gridded on a global cylindrical 25 km EASE-Grid 2.0 projection. Both ascending (morning) and descending (evening) pass data (provided in separate NetCDF files) are processed.

SMOS L3 brightness temperatures are provided at incidence angles in the range $\theta_j = \{2.5^\circ \text{ to } 62.5^\circ \text{ by } 5^\circ \text{ steps, and at } 40^\circ\}$. Not all incidence angles are provided at all pixels due to the sampling nature of the MIRAS radiometer onboard the SMOS satellite (Kerr et al. 2001), but in the retrieval algorithm used here we require at least 5 available incidence angles in order to generate a retrieval pair ($W_S, \rho_S$). This number of incidence angles was determined in Houtz et al. 2019 to eliminate many suspected false positive retrievals.

The Top-of-Atmosphere (TA) SMOS data is reformulated into Bottom-of-Atmosphere (BA) brightness temperatures according to the atmospheric correction first presented in Pellarin et al. 2003 and described in Houtz et al. 2019. The magnitude of the atmospheric correction ranges between about 2 K and 8 K depending on incidence angle.

### 2.4. Other satellite data products

We use data from the SSMI/S instrument aboard the Defense Meteorological Satellite Program (DMSP) F17 satellite, which are free to access from J. Mislanik 2004. These data are provided on a polar stereographic grid. SSMI/S has effective ground footprint sizes of 70 km × 45 km and 38 km × 30 km for the passive 19 GHz and 37 GHz channels, respectively, well comparable to the spatial resolution of SMOS L3 brightness temperatures. SSMI/S K- and Ka-band brightness temperatures are used to calculate the cross polarization gradient ratio or XPGR (Abdalati and Steffen 1995; Abdalati and Steffen 1997; Steffen et al. 1993), a frequently used freeze/thaw detection algorithm that provides a melt or no-melt flag based on an empirical threshold of the XPGR. The XPGR quantity is defined as,

$$\text{XPGR} \equiv \frac{T_{\text{B}}^{19\text{H}} - T_{\text{B}}^{37\text{V}}}{T_{\text{B}}^{19\text{H}} + T_{\text{B}}^{37\text{V}}}, \tag{9}$$

where $T_{\text{B}}^{19\text{H}}$ is the horizontal polarized brightness temperature measured at 19 GHz, and $T_{\text{B}}^{37\text{V}}$ is the vertical polarized brightness temperature measured at 37 GHz. With the XPGR algorithm, a pixel over the GrIS is determined to show melt if the XPGR quantity is above the threshold value of -0.0158 as determined in Abdalati and Steffen 1997. The period of SSMI/S data considered was from 2012 through 2016 corresponding to the other comparison datasets used.

Cryosat-2 surface elevation change data are taken from the CCI (Climate Change Initiative) ice sheet product described in Simonsen and Sørensen 2017. Cryosat-2 flies a Ku-band Synthetic Aperture Radar (SAR)/Interferometric Radar Altimeter instrument called SIRAL. SIRAL is capable of detection small changes in surface height with relative accuracy on centimeter scale. We use the 2012-2016 five-year average data, which are provided on a 10 km grid. The Cryosat-2 data are interpolated to the SMOS 25 km EASE-grid 2.0 cylindrical projection grid using two-dimensional spline interpolation in order to compare spatial patterns at comparable spatial resolutions.

Greenland mass balance products derived from GRACE satellite gravimetry are also obtained from the DTU (Technical University of Denmark) Space CCI ice sheet data product (Barletta et al. 2013). Though we also interpolate these data to the same SMOS 25 km grid, the true effective resolution of GRACE data is much coarser at about 250 km (Velicogna and Wahr 2013). We also use the 2012-2016 five-year average data from this product.

### 2.5. Greenland map and ice sheet mask

For our plots and mapping we use the Greenland Ice Mapping (GIMP) ice sheet mask (Howat et al. 2014) to discriminate ice sheet pixels from land or ocean. SMOS pixels are only considered in our analysis if the entirety of the EASE 2.0-grid pixel falls within the GIMP ice sheet mask. For this analysis the number $n_{\text{pixels}} = 2852$ within the GIMP ice sheet mask are considered. Pixels with mixed classification area (land/ocean/ice sheet) will likely lead to divergent retrievals, and thus we have excluded these pixels from the present study.

In the presented figures we use the high resolution Greenland coast outline provided in Greene et al. 2017. We also use other mapping related functions provided in Greene et al. 2017 for our analysis to convert latitude and longitudes to a polar-stereographic-north projection with units in meters so that interpolations are done on equi-distant units.

## 3. Results and discussion

### 3.1. Retrieved substrate brightness temperature and snow/firn density

The $T_0$ is the upwelling brightness temperature of the underlying substrate (glacial ice or layered firn/ice) which is estimated from the vertical polarization near-Brewster angle brightness temperatures as described in Eq. (3). $T_0$ is not necessarily the physical temperature of the ice because physical temperature gradients may exist within the substrate, and the permittivity may also be non-uniform if there are firn layers within the ice. Layered structures, coherence, roughness, and other effects may increase the substrate reflectivity beyond the calculated $s^p_{sub}$ such that $T_0$ becomes smaller. In Fig. 2 we present the (a) mean and (b) standard deviation of $T_0$, plotted over all of Greenland during the years 2012-2018. The year 2011 has been omitted from this plot because of high noise levels during the cold period (this can also be seen in the retrievals shown in Fig. 6). Upwelling substrate brightness temperatures of up to 260 K are found on the west coast of the southern half of Greenland where the standard deviations are also quite low. Low standard deviation of $T_0$ implies that the inter-annual changes of the firn/snow conditions atop the substrate have a small impact on the ice temperature. As the elevation increases, moving east from the southwest coast of the GrIS, $T_0$ decreases rapidly with nearly a 90 K gradient across a distance of a few hundred kilometers. This rapid decrease in $T_0$ is likely due to the increasing heterogeneity of the firn/ice transition, causing scattering and thus deviation from blackbody emission. As shown in Dunse et al. 2008; Harper et al. 2012, the transition from the bare-ice ablation zone to the percolation zone and accumulation zone is not a trivial, continuous, or smooth, transition in the upper ~10 meters. Rather, the firn/ice contains multiple layers of alternating firn and ice of varying densities.

In the percolation zone, liquid meltwater can reach depths down to 2 m (Samimi et al. 2020), whereas in the bare-ice ablation zone typical snowpack depth is less than this and water would sit atop glacial ice after percolating through the seasonal snowpack. In reality, the various regions of the GrIS are in constant flux, and each region has unique hydrological phenomena. The two-layer emission model aims to simplify GrIS hydrology by approximating the most common liquid water creation phenomenon, surface melt, over a dry snow/firn and ice structure.

The two-layer microwave emission model (LS-MEMLS in Fig. 1) used to retrieve ($W_S, \rho_S$) prescribes the substrate permittivity $\varepsilon_{sub}$ equal to the real part of homogeneous glacial ice. However, reality diverges from this idealization as a result of heterogeneities, particularly those in the transition between the firn and ice. Accordingly, the interpretation of measured vertical polarization brightness temperature close to the Brewster angle is not the physical temperature of ice. Rather, it is its effective upwelling brightness temperature that accounts for all radiative transfer mechanisms associated with its heterogeneity. The standard deviation of $T_0$ in this transition and percolation zone is expected to be higher because of the time-varying nature of the vertical firn/ice structures. At the higher elevations of the accumulation zone, in the dry snow regions, the standard deviation of $T_0$ is also low. This is because the vertical firn density gradient is approximately constant in time. Without percolating liquid water and various melt/refreeze cycles, the vertical structure in this region is spatially more uniform and less time variant. The spatial distributions of the cost function (*CF*) values show similar patterns to the standard deviation of $T_0$ suggesting that high values of this quantity indicate areas where the two-layer LS-MEMLS less accurately represents reality. The Greenland Ice Core Project (GRIP) core near the summit of the GrIS (72°34.74′N 37°33.92′W) found ice temperature of about 241 K (Dahl-Jensen et al. 1998) down to a depth beyond L-band sensitivity while our retrieval obtains $T_0$ near the GRIP site of 240 K. The largest standard deviations of $T_0$ are seen in the northern latitudes above ~76°N. This could be due to the relatively small amount of annual precipitation in this region where there is often blue ice at the surface and time-variant surface effects such as hummocks. Where the standard deviation of $T_0$ is low, or less than or equal to the instrumental noise standard deviation of ~3 K, we expect $T_0$ to correspond to the physical ice temperature at a depth depending on the

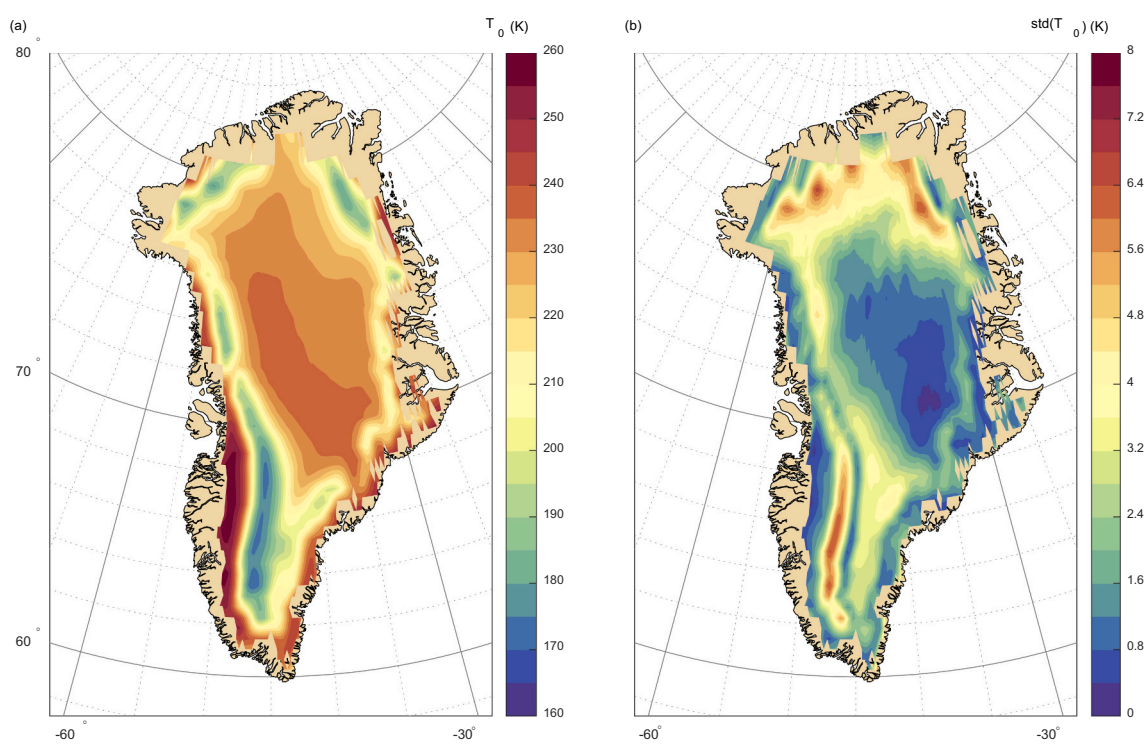


**Fig. 2.** (a) Mean retrieved upwelling substrate brightness temperature $T_0$ over years 2012-2018. (b) standard deviation std($T_0$) of annual upwelling substrate brightness temperatures.

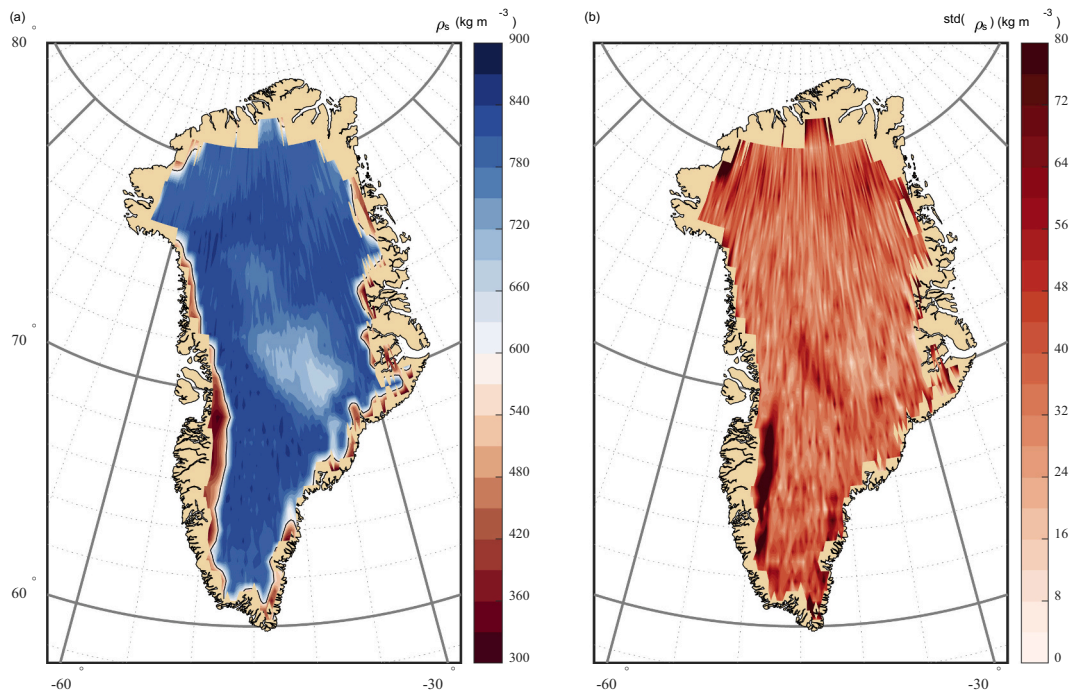


**Fig. 3.** (a) Mean retrieved snow/firn density $\rho_S$ (for $t_{wet}$ = 0.3 m) from 2011-2018 during dry snow period. The black contour line shows the estimated Equilibrium Line Altitude (ELA) contour of 600 kg m$^{-3}$. (b) Standard deviation std($\rho_S$) of retrieved snow/firn density from 2011-2018 during dry snow period.

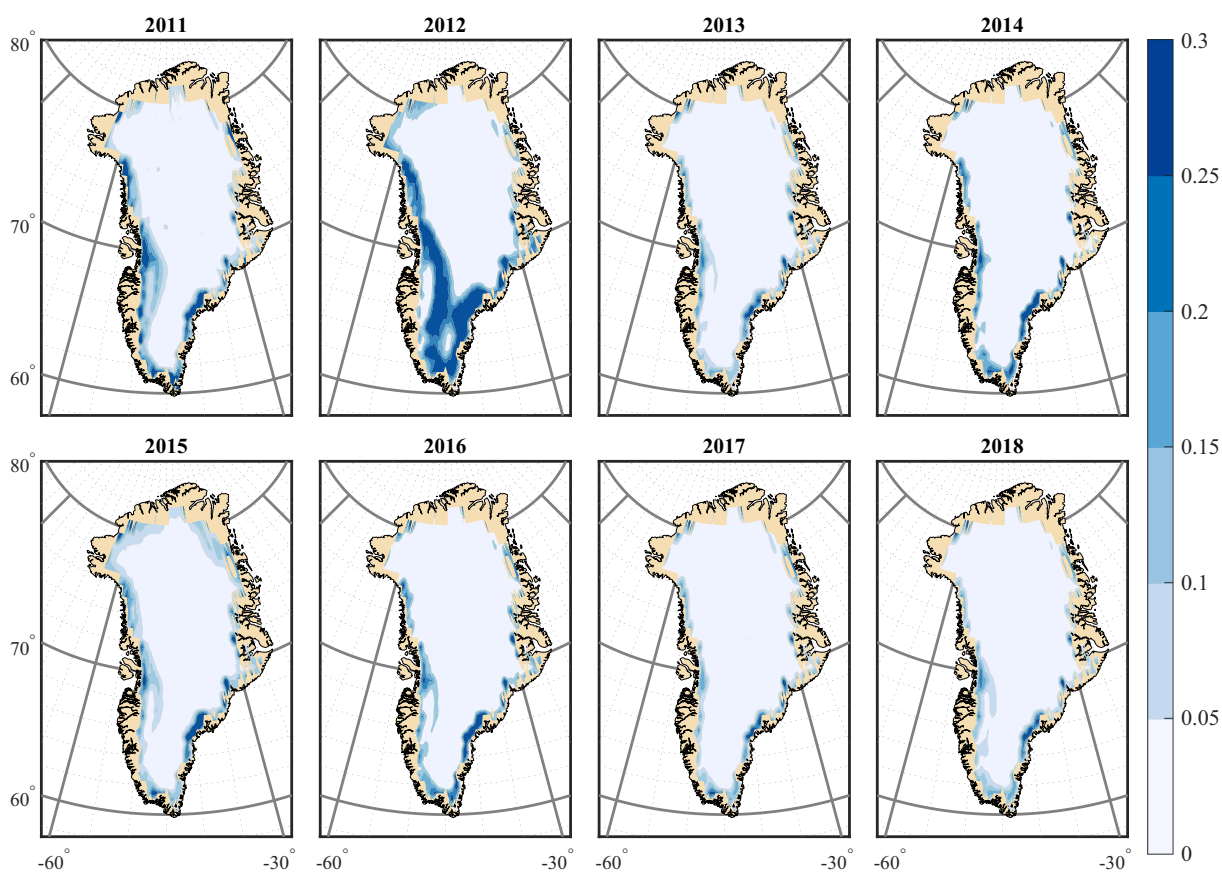


**Fig. 4.** Annual liquid water column $W_{c,\ yr}$ (m), down to L-band penetration depth, for years 2011 to 2018 calculated from SMOS $W_s$ retrievals for $t_{wet}$ = 0.3 m thickness of the upper firn/snow layer.

temperature profile and absorption coefficient of the ice.

Fig. 3 shows the mean and standard deviation of retrieved firn/snow density $\rho_S$ for the first 90-days of each year between 2011 and 2018 in subpanels (a) and (b), respectively. As was discussed in Houtz et al. 2019, the retrieved $\rho_S$ are more reasonable when considered during the dry snow period than during wet snow periods, and when considered as temporal averages rather than at instantaneous points in time. We see in Fig. 3(a) that in the coastal ablation zones, $\rho_S$ retrievals are on-the-order-of the mean density of a single season snowpack. Densities higher than ~600 kg m$^{-3}$ are typically reserved for multi-year firn. The density retrieved by inverting the two-layer LS-MEMLS (Fig. 1) is a weighted representative density of the firn/snow above the substrate defined as pure water ice ($\varepsilon_{sub} = 3.18$). The peak of this weighting was determined to be in the lowest ~10 cm of the snowpack for seasonal snow over soil (Naderpour et al. 2017), but this is a result of the clearly defined dielectric interface between snow and soil layers. We expect the case of the ablation zone, with a clear interface between ice and seasonal snow to be similar to the snow over soil case, but in the accumulation zone, the contrast between firn and ice is much less pronounced. Anyhow, a thorough sensitivity analysis based on knowledge of firn densification as a function of depth is required to determine the representative depth of $\rho_S$ for the various GrIS situations.

The black contour line at $\rho_S = 600$ kg m$^{-3}$, close to the ice edge, in Fig. 3(a) represents roughly the Equilibrium Line Altitude (ELA), or the transition from the bare-ice ablation zone, where the seasonal snowpack is completely melted each season, to the accumulation zone, where more precipitation accumulates than is melted. This is due to the lower mean density of a single-season snowpack as compared to firn. We expect to see larger relative temporal variations in the density of a seasonal snowpack than in the density of a deeper firn layer. This is consistent with what we see in the standard deviations std($\rho_S$) of the density shown in Fig. 3(b). Investigation of the time variation of the estimated ELA is beyond the scope of this study but will be approached in future work.

The contour plots in this section utilize a black line to indicate the land/ocean border of Greenland. The beige area indicates non-icesheet pixels, and the contours are plotted only on the pixels fully encapsulated by the GIMP ice sheet mask. The contours are plotted on the polar stereographic north projection.

### 3.2. Retrieved snow liquid water column and integrated surface liquid water

Presented in Fig. 4, are the annual liquid water columns $W_{c,\ yr}$ calculated from Eq. (5) and plotted as contour maps for years 2011-2018 for $t_{wet} = 0.3$ m. We see clearly the anomalous extensive melt of 2012. Previous works have documented this extreme melt year using a number of other satellite-based melt detection algorithms (Nghiem et al. 2012). It has been documented that there was even a brief period of melt over the entire GrIS, up to 3200 m above sea level (Bennartz et al. 2013). We do not see significant retrieved snow liquid water at the summit of the GrIS in July 2012, but we do see melt over a large portion of the ice sheet corroborating the findings of Nghiem et al. 2012. We can see differences in the spatial pattern of melt over different years. For example, in 2015 there was considerably more melt at the northern latitudes, and in 2011, 2014, and 2016 the south-eastern coast experienced more melt than during other years.

Fig. 5 shows the liquid water column over the dry snow period $W_{c,\ DoY=\{1-90\}}$ for the year 2016. Regions with significant non-zero water column during the assumed dry snow period suggests either; perennial liquid water storage by suspension in firn or aquifers, or false positive snow liquid water retrievals. Some of these regions correspond to locations that are known to have had perennial liquid water in 2016 (Miller et al. 2020), such as on the Eastern GrIS near 69° N, 33° W. The Jacobshavn ablation area on the West coast, not known to hold perennial liquid water, appears to provide some false positive liquid water retrievals during this period. This could be due to highly crevassed terrain, near the

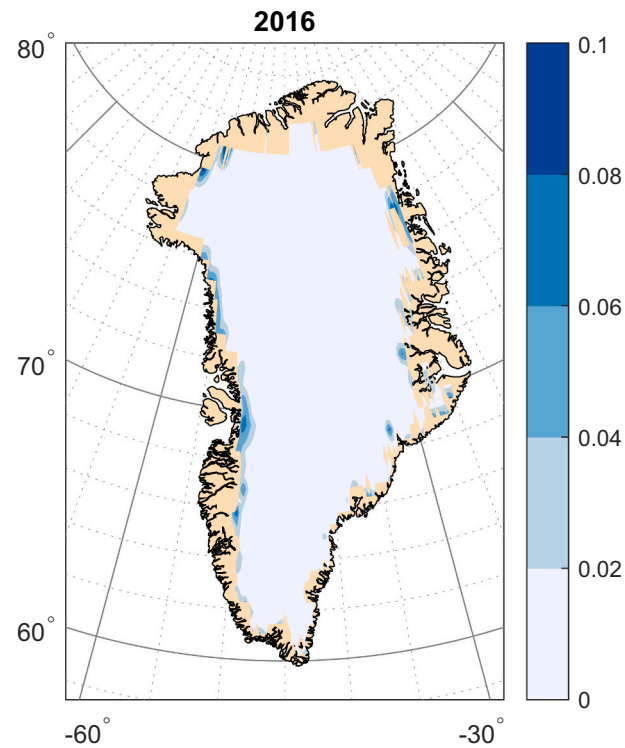


**Fig. 5.** Dry snow period liquid water column $W_{c,\ DoY\ =\ \{1-90\}}$ (m) down to L-band penetration depth for 2016, calculated from SMOS $W_s$ retrievals for $t_{wet} = 0.3$ m thickness of the upper firn/snow layer.

outlet glacier in this region, increasing reflectivity compared to the simple horizontal layers considered in the two-layer LS-MEMLS. The sum of the values of all the pixels in Fig. 5 is proportional the quantity $\sigma$ for each year, shown in Fig. 6, and provides a visualization of the spatial distribution of the contributions to this value.

Fig. 6 provides the time series of the daily integrated liquid water $W_{day}$, as well as a bar plot of the annual liquid water $W_{yr}$ over the GrIS calculated from Eq. (6) and (7), respectively. Values derived from retrievals $W_S$ for wet snow layer thicknesses of $t_{wet} = \{0.1, 0.3, 0.6, 1.0\}$ m are shown. The value of $\sigma$ used for computing Eq. (7) is computed for each year from Eq. (8), and is also plotted with $W_{day}$ in Fig. 6. The values of $W_{day}$ and $W_{yr}$ show a positive correlation on $t_{wet}$ suggesting that $t_{wet}$ is a tunable parameter, allowing calibration of the retrievals.

The annual liquid water $W_{yr}$ is the area under the curve of $W_{day}$ and above the annual mean noise value $\sigma$ (Eq. (8)), as seen in the grey shaded areas of $W_{day}$ ($t_{wet} = 0.3$ m) in Fig. 6. Thus, $\sigma$ has a significant influence on $W_{yr}$. $\sigma$ includes perennial (or at least present in the first 90 DoY) liquid water on, or within, the GrIS. The value of $W_{yr}$ only represents the change in L-band detectable liquid water between the first 90 DoY and the remainder of the year and thus, should represent the liquid water due to seasonal melt only, while neglecting detected perennial liquid water and false positive retrievals.

Uncertainty in model-derived surface mass balance estimates have been shown to be at least 60% (Ettema et al. 2009). Thus, accurate reference data with which to tune the retrieval algorithm is difficult to obtain. The effects of the assumptions, such as the simplified snowpack, and the summations (i) and (ii) in Section 2.2, contribute to the overall uncertainty of the liquid water estimate. Although, the presented algorithm provides advantages over alternative melt detection methods, particularly at higher microwave frequencies, where the EM is dependent on additional snow properties, including snow microstructure, which is difficult to accurately quantify, and spatially heterogeneous.

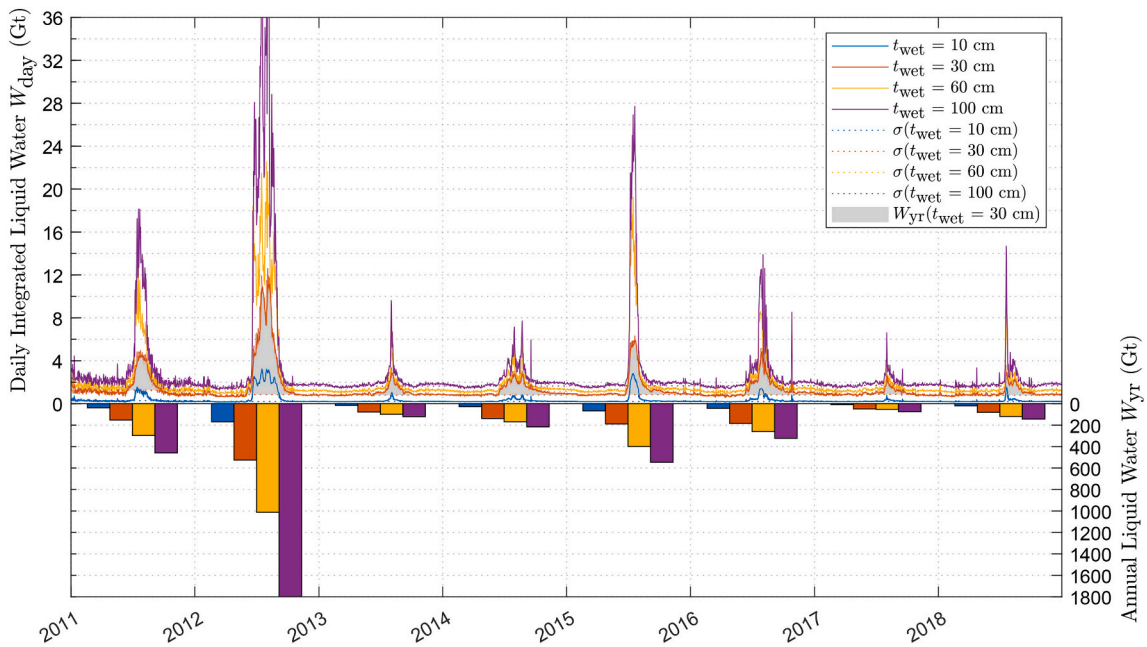


**Fig. 6.** Daily integrated liquid water $W_{day}$ on the upper left axis and annual liquid water $W_{yr}$ on the lower right axis computed from different modeled wet snow layer thicknesses $t_{wet} = \{0.1, 0.3, 0.6, 1.0\}$ m from 2011-2018. The mean noise levels $\sigma$ for the various modeled wet layer thicknesses are also plotted with dotted lines. The grey shaded regions indicate the area over which the sum for $W_{yr}$ for $t_{wet} = 0.3$ m (Eq. (7)) is performed, as an example.

### 3.3. Multi-satellite comparison

In Fig. 7 we have plotted 5 year means, from 2012-2016, of the following: (a) the average annual liquid water column derived from SMOS for $t_{wet} = 0.3$ m, (b) the average total number of annual melt days from the XPGR algorithm, (c) the average annual surface elevation decrease from Cryosat-2 and, (d) the average annual mass loss from the Greenland mass balance product from GRACE. Upon initial comparison, the four contours show similar spatial patterns, although there are some notable differences between these individual indicators.

Recent estimates predict that surface melt water runoff contributes to about 52% of the total mass loss of Greenland (Andrew et al. 2019). The GRACE data product measures total mass balance (accounting for losses due to surface losses, glacier discharge, plus gains due to precipitation) because it is measuring changes in gravity related to mass distribution, while the 19/37 GHz passive-microwave-based methods (such as XPGR) are expected to be indicators of surface melt only. Glacier discharge can also cause thinning and affect surface height, particularly around outlet glaciers, which would also be seen in the Cryosat-2 height change data. While gravimetry from GRACE is likely the most direct measurement of total mass balance, the spatial and temporal resolution of these measurements is quite limited. It is also often desirable, for hydrology or glacier dynamics applications, to be able to separate discharge from surface mass loss contributions.

Our SMOS algorithm captures significant melt near the Jacobshavn outlet glacier at about 69° N near the West coast, also seen in the height change signature. The SMOS algorithm shows little to no melt near South Dome (~2900 m above sea level, 63° N), the highest point on the southern part of the ice sheet. The $W_{c,yr}$ contours then roughly follow the elevation isolines indicating that the melt increases with decreasing altitude. Both the SMOS and XPGR algorithms detect significant melt near the southeast coast that are not seen as significantly neither in the height change (Cryosat-2) nor in the mass balance (GRACE) data. Although the SMOS and XPGR melt algorithms suggest there is significant melt in this area, this is also an area of high precipitation, which adds both mass and height.

Due to the simplistic two-layer LS-MEMLS, which assumes the existence of a snowpack, the algorithm may underestimate liquid water volume over large areas (on the order of a SMOS pixel) of standing liquid water such as supra-glacial lakes. If lakes are much deeper than the penetration depth of L-band in water, ~1 cm, then more water below this will no longer influence the measured brightness temperature of a pixel, effectively causing a brightness temperature saturation. The maximum $W_S$ retrieved for $t_{wet} = 0.3$ m over 2011-2018 is 0.225 $m^3m^{-3}$. This corresponds to a water column $W_{c,i}$ of about 0.07 m (7 cm). For wet snow, it was shown in Mätzler et al. 1980 that brightness temperature continues to decrease nearly linearly with increasing water content. This suggests that mixed-pixels containing areal fractions of wet snow and standing water will result in proportionally higher $W_S$ retrievals and corresponding larger average water column over the pixel.

A second effect that leads our SMOS-based algorithm to underestimate the liquid water present on the ice sheet is the masking of near-coast pixels. Ablation and melt increase exponentially nearer to the coasts (Broeke et al. 2008), while up to 25 km of the ice sheet nearest to the coasts is being masked out of the SMOS data. While these two effects lead to the tendency to underestimate total liquid water, there are two opposing effects favoring an overestimation or positive bias.

Impacts causing the SMOS-based retrievals to overestimate the total liquid water are related to multiple detections of the same volume of liquid water. By summing up all the SMOS-detected liquid water we are introducing two potential biases that would increase the retrieved liquid water volume as compared to the true liquid water present on the GrIS. If liquid water sits suspended in snow, lakes, or firn, without percolating or draining, our SMOS detection algorithm could detect this same volume of water multiple times and the column integration (Eq. (5) and Eq. (6)) will add it each time it is detected by SMOS. The total liquid water is not the same as the meltwater runoff due to refreezing, evaporation and sublimation as well as liquid water retention in firn and sub-surface aquifers. In order to estimate meltwater runoff, and thus SMB, using SMOS-based retrievals, one must have accurate knowledge of these terms. While acknowledging the potential biases and error sources, we make comparisons of the SMOS-based annual liquid water $W_{yr}$ with model-based estimates of total liquid water or melt.

There are two additional possible sources of uncertainty. Radiative cooling of the snow surface during clear skies could refreeze liquid water at the surface and thus reduce the surface reflectivity of the wet snow

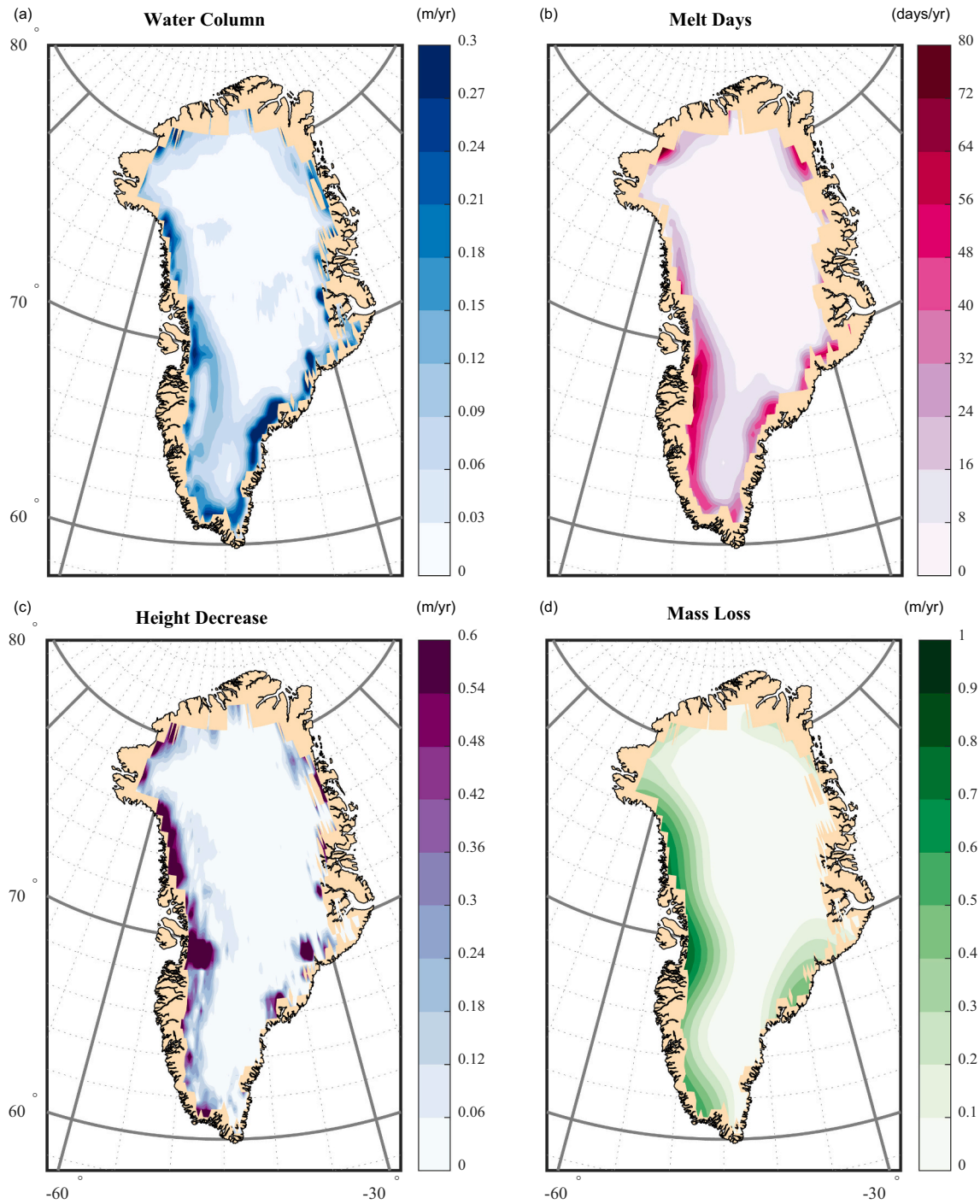


**Fig. 7.** Annual average from 2012-2016 of (a) annual liquid water column $W_{c,\ yr}$ ($t_{wet}$ = 0.3 m) derived from SMOS (m/yr), (b) annual number of melt days from SSMI/S and XPGR algorithm (days/yr), (c) surface elevation decrease from Cryosat2 (m/yr), (d) mass loss from GRACE (water equivalent m/yr).

due to an impedance matching effect. The radiative cooling effect causes an underestimation of snow liquid water content during clear sky weather. An additional uncertainty contributor is introduced in the rare event of rain on the GrIS. If all liquid water on the GrIS is assumed to be a result of melt, then rain water present on the GrIS surface would cause an overestimation of melt.

Separating surface mass loss due to runoff and sublimation/evaporation from gains due to precipitation is more difficult when using direct gravimetry or height change measurements. The SMOS-based algorithm provides an independent measure of the surface liquid water on the GrIS which is the dominant term in the SMB due to runoff of this liquid water. About 45% of the melt water refreezes, but runoff accounts for 90% of the total surface loss, while both evaporation and sublimation account for 10% (Ettema et al. 2009). The SMOS-based retrieval algorithm provides a direct measurement of liquid water that, thus far, has only been accessible by climatological modeling. The state-dependent and spatially variable penetration depth of L-band microwaves over the GrIS may constrain the practical usability of the retrieval algorithm for direct climate assessment, but contributes an important piece of information for climate modeling.

Estimates of the total mass balance change of the GrIS (Eq. (1)), based on comprehensive analyses from GRACE and climate modeling,

**Table 2**
Comparison of GrIS total melt from SMOS-based retrievals and published model values

| source | 2012 total melt (Gt) | mean period | mean total melt (Gt) |
|---|---|---|---|
| Model Van Angelen et al. 2014 | 1043 | 2007-2012 | 751 |
| Model Forecast (Mernild et al. 2010 | - | 2010-2019 | 593 |
| SMOS $t_{wet} = 0.1$ m | 169 | 2011-2018 | 49 |
| SMOS $t_{wet} = 0.3$ m | 525 | 2011-2018 | 175 |
| SMOS $t_{wet} = 0.6$ m | 1012 | 2011-2018 | 301 |
| SMOS $t_{wet} = 1.0$ m | 1800 | 2011-2018 | 460 |

range from -239±20 Gt/yr between 2012 and 2017 (Andrew et al. 2019) to -286±20 Gt/yr between 2010-2018 (Mouginot et al. 2019). It is also estimated that between 52% (Andrew et al. 2019) and 60% (Flowers 2018) of the total mass loss (neglecting the positive precipitation term) is due to increased surface melt and meltwater runoff. It has also been calculated from climate modeling that the 1958-2007 average annual total amount of liquid water on the ice sheet was 450 Gt/yr (Ettema et al. 2009), or 480 Gt/yr for the period of 1960-2014 (Steger et al. 2017). Other model-based results suggest total melt in 2012 was equal to 1043 Gt/yr, or the 2007-2012 average was 751 Gt/yr (Van Angelen et al. 2014). A forecast model predicted in 2010 that the mean of 2010-2019 total liquid water would have a value of 593 Gt/yr (Mernild et al. 2010). The average $W_{yr}$ for different $t_{wet}$ values are presented in Table 2 along with the total liquid water/melt values available in the literature from climate modeling.

The SMOS-based retrievals show an underestimation when compared to model predictions of total melt water, likely caused by the mechanisms discussed above. By applying corrections for the limited penetration depth due to saturation, near-coast pixels, percolation rate, as well as refreezing and evaporation, SMOS retrievals could potentially estimate the meltwater runoff mass loss of the GrIS. The most comprehensive use of SMOS-based liquid water retrievals will likely be in combination with mass-balance models, energy balance models, and meteorological reanalysis data.

The challenge of using gravimetry to estimate mass change is that it takes a long time to collect enough data to achieve a meaningful estimate of mass change, hence the five-year averages presented here. Using surface elevation change to estimate mass balance also has its difficulties because snow and firn density is a significant unknown, and additional effects, such as isostatic rebound (the tectonic lifting of the bedrock as mass is removed) also contribute uncertainty. With sensitivity to liquid water column, L-band radiometry provides an important addition to the field of GrIS melt and surface mass balance study.

## 4. Conclusions

Our study demonstrated the feasibility of SMOS-based $W_s$ and $\rho_s$ retrievals over the GrIS, and the potential to map the ELA and estimate surface mass losses. This was the first use of L-band radiometry to obtain melt data over the entire GrIS. The new algorithm was recently introduced in Houtz et al. 2019, validated in Naderpour et al. 2020, and demonstrated the validity of the retrievals over a single site including a comparison to in-situ temperature data, and a comparison with the XPGR melt detection algorithm. We have now shown that a simple two-layer snowpack, input to the LS-MEMLS forward model, provides an approximation of the near-surface physics of the entire GrIS sufficient for inversion in the retrieval algorithm. We have demonstrated the spatial and temporal trends of retrieved parameters including: the effective substrate temperature, mean winter firn/snow density, snow liquid water content, water column, and surface liquid water.

The SMOS-based liquid water ($W_{day}$ and $W_{yr}$) estimates offer a unique and new insight into melt water quantification and surface mass loss over the GrIS. In contrast to previous passive-microwave-based melt characterization techniques, the SMOS-based algorithm allows quantification of liquid water volume instead of only mapping melt extent. We found that the SMOS-based $W_c$ retrievals can be tuned by the wet snow layer thickness, the only non-deterministic parameter in two-layer LS-MEMLS. It was demonstrated that multi-angle L-band brightness temperatures are sensitive to liquid water column down to the L-band penetration depth, and this can be retrieved from inversion of the physical LS-MEMLS. Further analysis will obtain an optimal wet layer thickness value, or investigate use of a spatially variable wet layer thickness over different regions of the GrIS. A further sensitivity analysis will aim to quantify the discussed uncertainty sources, particularly the saturating effect due to decreased L-band penetration depth with increased liquid water content.

L-band microwaves (at 1.4 GHz), as opposed to higher frequency passive microwaves (such as 19 GHz and 37 GHz), have a deeper penetration depth into snow and ice, which suggests that L-band radiometry provides different and complementary information. Firstly, higher frequencies lose penetration at much lower snow liquid water contents, thus why they have only been used for surface melt flagging as opposed to liquid water quantification. Secondly, the deeper penetration of L-band microwaves in dry snow and firn suggests that SMOS can see subsurface water suspended in firn. Use of L-band radiometry for melt and liquid water detection over the GrIS is a natural addition to the already available methods and will likely lead to improved SMB estimation.

It was demonstrated that it is possible to estimate GrIS surface liquid water using L-band radiometry, but this estimate could be improved by introduction of percolation and melt water runoff models to better describe the path of liquid water and the thickness of the wet snow layer, and corrections to near-coastal areas and saturated pixels. A percolation model to describe the path of meltwater as a function of time, temperature, and snowpack properties would allow more accurate calculation of $W_{day}$ and $W_{yr}$ from retrieved $W_s$. A percolation and meltwater evolution model would allow theoretical validation of the assumptions made in the summations of annual liquid water and water column, and allow quantification of the uncertainty terms leading to over- and underestimation. We also intend to validate the near-linear decrease of brightness temperature, and thus constant sensitivity to liquid water, for large values of liquid water content and pixels with mixed contributions from wet snow and standing water.

Investigation of the effect of the imaginary part of ice permittivity, and the impact of bedrock at low ice sheet altitudes are two additional parameters that need further investigation (Pablos et al. 2015). A future study to compare liquid water retrievals with various passive and active microwave melt retrieval techniques over all of Greenland is also a natural follow-on study. We also anticipate an upcoming study comparing the SMOS-based retrievals with snow liquid water calculated from snowpack evolution/energy budget models from the many in-situ Automatic Weather Stations (AWS) across the GrIS.

Various unknowns remain relating to the SMOS-based GrIS retrievals, particularly, the uncertainty and sensitivity to the possible errors and assumptions previously mentioned. Further sensitivity analysis will investigate mixed pixel (water/snow or bare ice/snow) behavior, behavior of retrievals under saturation, and the underestimation impact of multiple measurements of the same water volume. Use of a firn model would also improve the accuracy and usability of the $\rho_s$ retrievals in the accumulation zone.

## Declaration of Competing Interest

The authors declare that they have no known competing financial

interests or personal relationships that could have appeared to influence the work reported in this paper.

## Acknowledgements

Part of this study was funded by the "European Space Agency" (ESA) within the "SMOS Expert Support Laboratory (ESL) for Level-2 Soil Moisture" contract (No.: 4000125649) with "GAMMA Remote Sensing Research and Consulting AG (3073 Gümligen, Switzerland)". Part of this study was funded by the Swiss National Science Foundation (SNF) project "Active/Passive REmote Sensing of Snow" (APRESS), contract number 200020L_182049. The remaining contribution was from the "Swiss Federal Institute WSL" (8903 Birmensdorf, Switzerland).

## References

Abdalati, W., Steffen, K., 1995. Passive microwave-derived snow melt regions on the Greenland ice sheet. Geophysical research letters 22, 787–790.
Abdalati, W., Steffen, K., 1997. Snowmelt on the Greenland ice sheet as derived from passive microwave satellite data. Journal of Climate 10, 165–175.
Al Bitar, A., Mialon, A., Kerr, Y.H., Cabot, F., Richaume, P., Jacquette, E., Quesney, A., Mahmoodi, A., Tarot, S., Parrens, M., 2017. The global SMOS Level 3 daily soil moisture and brightness temperature maps. Earth System Science Data 9, 293–315.
Andrew, S., Erik, I., Eric, R., Ben, S., van den Broeke, M., Isabella, V., Pippa, W., Kate, B., Ian, J., Gerhard, K., 2019. Mass balance of the Greenland Ice Sheet from 1992 to 2018.
Barletta, V.R., Sabadini, R., Bordoni, A., 2008. Isolating the PGR signal in the GRACE data: impact on mass balance estimates in Antarctica and Greenland. Geophysical Journal International 172, 18–30.
Barletta, V.R., Sørensen, L.S., Forsberg, R., 2013. Scatter of mass changes estimates at basin scale for Greenland and Antarctica. Cryosphere 7, 1411–1432.
Bennartz, R., Shupe, M., Turner, D., Walden, V., Steffen, K., Cox, C., Kulie, M., Miller, N., Pettersen, C., 2013. Greenland melt extent enhanced by low-level liquid clouds. Nature 496, 83.
Brangers, I., Lievens, H., Miege, C., Demuzere, M., Brucker, L., De Lannoy, G., 2020. Sentinel-1 Detects Firn Aquifers in the Greenland Ice Sheet. Geophysical research letters *47* e2019GL085192.
Brodzik, M.J., Billingsley, B., Haran, T., Raup, B., Savoie, M.H., 2012. EASE-Grid 2.0: Incremental but significant improvements for Earth-gridded data sets. ISPRS International Journal of Geo-Information 1, 32–45.
Broeke, M., Smeets, P., Ettema, J., Veen, C., Wal, R., Oerlemans, J., 2008. Partitioning of melt energy and meltwater fluxes in the ablation zone of the west Greenland ice sheet. The Cryosphere 2, 179–189.
van den Broeke, M., Box, J., Fettweis, X., Hanna, E., Noël, B., Tedesco, M., van As, D., van de Berg, W.J., van Kampenhout, L., 2017. Greenland ice sheet surface mass loss: Recent developments in observation and modeling. Current Climate Change Reports 3, 345–356.
Dahl-Jensen, D., Mosegaard, K., Gundestrup, N., Clow, G.D., Johnsen, S.J., Hansen, A.W., Balling, N., 1998. Past temperatures directly from the Greenland ice sheet. Science 282, 268–271.
Dunse, T., Eisen, O., Helm, V., Rack, W., Steinhage, D., Parry, V., 2008. Characteristics and small-scale variability of GPR signals and their relation to snow accumulation in Greenland's percolation zone. Journal of Glaciology 54, 333–342.
Entekhabi, D., Njoku, E.G., O'Neill, P.E., Kellogg, K.H., Crow, W.T., Edelstein, W.N., Entin, J.K., Goodman, S.D., Jackson, T.J., Johnson, J., Kimball, J., Piepmeier, J.R., Koster, R.D., Martin, N., McDonald, K.C., Moghaddam, M., Moran, S., Reichle, R., Shi, J.C., Spencer, M.W., Thurman, S.W., Tsang, L., & Van Zyl, J. (2010). The Soil Moisture Active Passive (SMAP) Mission. *Proceedings of the IEEE, 98*, 704-716.
Ettema, J., van den Broeke, M.R., van Meijgaard, E., van de Berg, W.J., Bamber, J.L., Box, J.E., Bales, R.C., 2009. Higher surface mass balance of the Greenland ice sheet revealed by high-resolution climate modeling. Geophysical research letters 36.
Flowers, G.E., 2018. Hydrology and the future of the Greenland Ice Sheet. Nature Communications 9, 2729.
Forsberg, R., Sørensen, L., Simonsen, S., 2017. Greenland and Antarctica ice sheet mass changes and effects on global sea level. In: Integrative Study of the Mean Sea Level and Its Components. Springer, pp. 91–106.
Gillet-Chaulet, F., Gagliardini, O., Seddik, H., Nodet, M., Durand, G., Ritz, C., Zwinger, T., Greve, R., Vaughan, D.G., 2012. Greenland ice sheet contribution to sea-level rise from a new-generation ice-sheet model. The Cryosphere 6, 1561–1576.
Golledge, N.R., Keller, E.D., Gomez, N., Naughten, K.A., Bernales, J., Trusel, L.D., Edwards, T.L., 2019. Global environmental consequences of twenty-first-century ice-sheet melt. Nature 566, 65–72.
Greene, C.A., Gwyther, D.E., Blankenship, D.D., 2017. Antarctic mapping tools for MATLAB. Computers & Geosciences 104, 151–157.
Hall, D.K., Comiso, J.C., DiGirolamo, N.E., Shuman, C.A., Box, J.E., Koenig, L.S., 2013. Variability in the surface temperature and melt extent of the Greenland ice sheet from MODIS. Geophysical research letters 40, 2114–2120.
Harper, J., Humphrey, N., Pfeffer, W.T., Brown, J., Fettweis, X., 2012. Greenland ice-sheet contribution to sea-level rise buffered by meltwater storage in firn. Nature 491, 240.
Houtz, D., Naderpour, R., Schwank, M., Steffen, K., 2019. Snow wetness and density retrieved from L-band satellite radiometer observations over a site in the West Greenland ablation zone. Remote Sensing of Environment 235, 111361.
Howat, I., Negrete, A., Smith, B., 2014. The Greenland Ice Mapping Project (GIMP) land classification and surface elevation data sets. The Cryosphere 8, 1509–1518.
Hurkmans, R., Bamber, J., Davis, C., Joughin, I., Khvorostovsky, K., Smith, B., Schoen, N., 2014. Time-evolving mass loss of the Greenland Ice Sheet from satellite altimetry. The Cryosphere 8, 1725–1740.
Kerr, Y.H., Waldteufel, P., Wigneron, J.P., Martinuzzi, J.M., Font, J., Berger, M., 2001. Soil moisture retrieval from space: The Soil Moisture and Ocean Salinity (SMOS) mission. IEEE Transactions on Geoscience and Remote Sensing 39, 1729–1735.
Kopp, R.E., Kemp, A.C., Bittermann, K., Horton, B.P., Donnelly, J.P., Gehrels, W.R., Hay, C.C., Mitrovica, J.X., Morrow, E.D., & Rahmstorf, S. (2016). Temperature-driven global sea-level variability in the Common Era. *Proceedings of the National Academy of Sciences, 113*, E1434-E1441.
Luo, Z., Li, Q., Zhang, K., Wang, H., 2012. Trend of mass change in the Antarctic ice sheet recovered from the GRACE temporal gravity field. Science China Earth Sciences 55, 76–82.
Macelloni, G., Leduc-Leballeur, M., Brogioni, M., Ritz, C., Picard, G., 2016. Analyzing and modeling the SMOS spatial variations in the East Antarctic Plateau. Remote Sensing of Environment 180, 193–204.
Maslanik, J., J.S., 2004. DMSP SSM/I-SSMIS Daily Polar Gridded Brightness Temperatures, Version 4. Boulder, Colorado USA. NASA National Snow and Ice Data Center Distributed Active Archive Center.
Mätzler, C., 2001. Applications of SMOS over terrestrial ice and snow. In: Prepared for 3rd SMOS Workshop, DLR, Oberpfaffenhofen, Germany, December 10-12, 2001.
Matzler, C., Schanda, E., Hofer, R., Good, W., Rango, A., 1980. Microwave signatures of the natural snow cover at Weissfluhjoch. In: NASA Conference Publication, p. 203.
Mätzler, C., Aebischer, H., Schanda, E., 1984. Microwave Dielectric-Properties of Surface Snow. IEEE Journal of Oceanic Engineering 9, 366–371.
Mernild, S.H., Liston, G.E., Hiemstra, C.A., Christensen, J.H., 2010. Greenland ice sheet surface mass-balance modeling in a 131-yr perspective, 1950–2080. Journal of Hydrometeorology 11, 3–25.
Miège, C., Forster, R.R., Brucker, L., Koenig, L.S., Solomon, D.K., Paden, J.D., Box, J.E., Burgess, E.W., Miller, J.Z., McNerney, L., 2016. Spatial extent and temporal variability of Greenland firn aquifers detected by ground and airborne radars. Journal of Geophysical Research: Earth Surface 121, 2381–2398.
Miller, J.Z., Long, D.G., Jezek, K.C., Johnson, J.T., Brodzik, M.J., Shuman, C.A., Koenig, L.S., Scambos, T.A., 2020. Brief communication: Mapping Greenland's perennial firn aquifers using enhanced-resolution L-band brightness temperature image time series. The Cryosphere 14, 2809–2817.
Moore, P., King, M.A., 2008. Antarctic ice mass balance estimates from GRACE: Tidal aliasing effects. Earth Surface, Journal of Geophysical Research, p. 113.
Mouginot, J., Rignot, E., Bjørk, A.A., van den Broeke, M., Millan, R., Morlighem, M., Noël, B., Scheuchl, B., Wood, M., 2019. Forty-six years of Greenland Ice Sheet mass balance from 1972 to 2018. Proceedings of the National Academy of Sciences *116*, 9239–9244.
Naderpour, R., Schwank, M., Matzler, C., 2017. Davos-Laret Remote Sensing Field Laboratory: 2016/2017 Winter Season L-Band Measurements Data-Processing and Analysis. Remote Sensing 9, 1185.
Naderpour, R., Houtz, D., Schwank, M., 2020. Snow Wetness Retrieved from Close-Range L-band Radiometry in the Western Greenland Ablation Zone. J. of Glaciology. In Review.
Nerem, R.S., Beckley, B.D., Fasullo, J.T., Hamlington, B.D., Masters, D., Mitchum, G.T., 2018. Climate-change–driven accelerated sea-level rise detected in the altimeter era. Proceedings of the National Academy of Sciences *115*, 2022–2025.
Nghiem, S., Steffen, K., Kwok, R., Tsai, W., 2001. Detection of snowmelt regions on the Greenland ice sheet using diurnal backscatter change. Journal of Glaciology 47, 539–547.
Nghiem, S., Hall, D., Mote, T., Tedesco, M., Albert, M., Keegan, K., Shuman, C., DiGirolamo, N., Neumann, G., 2012. The extreme melt across the Greenland ice sheet in 2012. Geophysical research letters 39.
Oppenheimer, M., Glavovic, B.C., Hinkel, J., Wal, R.V.D., Magnan, A.K., Abd-Elgawad, A., Cai, R., CifuentesJara, M., DeConto, R.M., Ghosh, T., Hay, J., Isla, F., Marzeion, B., Meyssignac, B., Sebesvari, Z., 2019. 2019: Sea Level Rise and Implications for Low-Lying Islands, Coasts and Communities. IPCC Special Report on the Ocean and Cryosphere in a Changing Climate.
Pablos, M., Piles, M., González-Gambau, V., Camps, A., Vall-llossera, M., 2015. Ice thickness effects on Aquarius brightness temperatures over Antarctica. Journal of Geophysical ResearchOceans *120*, 2856–2868.
Pellarin, T., Wigneron, J.P., Calvet, J.C., Berger, M., Douville, H., Ferrazzoli, P., Kerr, Y. H., Lopez-Baeza, E., Pulliainen, J., Simmonds, L.P., Waldteufel, P., 2003. Two-year global simulation of L-band brightness temperatures over land. IEEE Transactions on Geoscience and Remote Sensing 41, 2135–2139.
Rignot, E., Echelmeyer, K., Krabill, W., 2001. Penetration depth of interferometric synthetic-aperture radar signals in snow and ice. Geophysical research letters 28, 3501–3504.
Rignot, E., Box, J., Burgess, E., Hanna, E., 2008. Mass balance of the Greenland ice sheet from 1958 to 2007. Geophysical research letters 35.
Samimi, S., Marshall, S.J., 2017. Diurnal cycles of meltwater percolation, refreezing, and drainage in the supraglacial snowpack of Haig glacier, Canadian Rocky Mountains. Frontiers in Earth Science 5, 6.
Samimi, S., Marshall, S.J., MacFerrin, M., 2020. Meltwater Penetration Through Temperate Ice Layers in the Percolation Zone at DYE-2. Greenland Ice Sheet. *Geophysical research letters 47* e2020GL089211.

Schwank, M., Rautiainen, K., Matzler, C., Stahli, M., Lemmetyinen, J., Pulliainen, J., Vehvilainen, J., Kontu, A., Ikonen, J., Menard, C.B., Drusch, M., Wiesmann, A., Wegmuller, U., 2014. Model for microwave emission of a snow-covered ground with focus on L band. Remote Sensing of Environment 154, 180–191.

Simonsen, S.B., Sørensen, L.S., 2017. Implications of changing scattering properties on Greenland ice sheet volume change from Cryosat-2 altimetry. Remote Sensing of Environment 190, 207–216.

Steffen, K., 1995. Surface energy exchange at the equilibrium line on the Greenland ice sheet during onset of melt. Annals of Glaciology 21, 13–18.

Steffen, K., Abdalati, W., Stroeve, J., 1993. Climate sensitivity studies of the Greenland ice sheet using satellite AVHRR, SMMR, SSM/I and in situ data. Meteorology and Atmospheric Physics 51, 239–258.

Steger, C.R., Reijmer, C.H., van den Broeke, M.R., 2017. The modelled liquid water balance of the Greenland Ice Sheet. Cryosphere 11, 2507–2526.

Van Angelen, J., Van den Broeke, M., Wouters, B., Lenaerts, J., 2014. Contemporary (1960–2012) evolution of the climate and surface mass balance of the Greenland ice sheet. Surveys in Geophysics 35, 1155–1174.

Velicogna, I., Wahr, J., 2005. Greenland mass balance from GRACE. Geophysical research letters 32.

Velicogna, I., Wahr, J., 2013. Time-variable gravity observations of ice sheet mass balance: Precision and limitations of the GRACE satellite data. Geophysical research letters 40, 3055–3063.

van der Wal, W., Whitehouse, P.L., Schrama, E.J., 2015. Effect of GIA models with 3D composite mantle viscosity on GRACE mass balance estimates for Antarctica. Earth and Planetary Science Letters 414, 134–143.